communications earth & environment

ARTICLE

https://doi.org/10.1038/s43247-023-00839-w OPEN

Satellite-observed strong subtropical ocean warming as an early signature of global warming

Hu Yang[1,2✉], Gerrit Lohmann[1,3], Christian Stepanek[1], Qiang Wang[1], Rui Xin Huang[4], Xiaoxu Shi[1,2], Jiping Liu[2,5], Dake Chen[2], Xulong Wang[6,7], Yi Zhong[8], Qinghua Yang[2,5], Ying Bao[9] & Juliane Müller[1,3]

Satellite observations covering the last four decades reveal an ocean warming pattern resembling the negative phase of the Pacific Decadal Oscillation. This pattern has therefore been widely interpreted as a manifestation of natural climate variability. Here, we re-examine the observed warming pattern and find that the predominant warming over the subtropical oceans, while mild warming or even cooling over the subpolar ocean, is dynamically consistent with the convergence and divergence of surface water. By comparison of observations, paleo-reconstructions, and model simulations, we propose that the observed warming pattern is likely a short-term transient response to the increased CO_2 forcing, which only emerges during the early stage of anthropogenic warming. On centennial to millennial timescales, the subpolar ocean warming is expected to exceed the temporally dominant warming of the subtropical ocean. This delayed but amplified subpolar ocean warming has the potential to reshape the ocean-atmosphere circulation and threaten the stability of marine-terminating ice sheets.

[1] Alfred Wegener Institute, Helmholtz Centre for Polar and Marine Research, Bremerhaven, Germany. [2] Southern Marine Science and Engineering Guangdong Laboratory (Zhuhai), Zhuhai, China. [3] Center for Marine Environmental Sciences, MARUM, University of Bremen, Bremen, Germany. [4] Woods Hole Oceanographic Institution, Woods Hole, USA. [5] School of Atmospheric Sciences, Sun Yat-sen University, Zhuhai, China. [6] State Key Laboratory of Loess and Quaternary Geology, Institute of Earth Environment, Chinese Academy of Sciences, Xi'an, China. [7] CAS Center for Excellence in Quaternary Science and Global Change, Chinese Academy of Sciences, Xi'an, China. [8] Centre for Marine Magnetism, Department of Ocean Science and Engineering, Southern University of Science and Technology, Shenzhen, China. [9] First Institute of Oceanography, Ministry of Natural Resources, Qingdao, China. ✉email: yanghu@sml-zhuhai.cn

In the past century, and particularly in the past few decades, the concentration of greenhouse gases (GHG) in the atmosphere has increased at an unprecedented rate[1], causing widespread warming and climate changes[2]. Toward planning adaptation measures, we are eager to know: how much warming we can anticipate as a result of rising GHG? And what is the current status of global warming? Given that the ocean is the primary absorber of the anomalous heat trapped by rising GHG[3], evaluating ocean warming will promote our understanding of these two questions.

The International Comprehensive Ocean-Atmosphere Data Set (ICOADS) provides the longest ocean temperature data, spanning more than three centuries[4]. However, these data are collected primarily by commercial vessels, resulting in uncertainties due to inconsistencies in sampling frequency, location, and methodology[5,6]. The quality of ocean temperature records has largely improved thanks to satellite observations, which have recently reached a milestone of forty years of temporal coverage[7]. The ocean warming pattern obtained from satellites reveals several intriguing features. Accelerated warming is identified over the subtropical extension of oceanic western boundary currents[8], while a cold patch is found over the subpolar North Atlantic Ocean. The former is explained as a result of intensification and poleward shift of oceanic western boundary currents[9], whereas the latter is likely linked to a weakening of the Atlantic Meridional Overturning Circulation[10–12]. On a hemispheric scale, the warming of the Northern Hemisphere is stronger than that of the Southern Hemisphere[13–17]. Over the Southern Ocean, a slight cooling is detected, likely related to the anomalous expansion of sea ice[18–20], upwelling of pristine deepwater[17,21], and/or Antarctic ozone depletion[22–25]. Apart from these well-identified features, the dominant large-scale warmings are found in subtropical latitudes.

In this study, the satellite-observed ocean warming pattern is compared with the reconstructed mid-Pliocene sea surface temperature (SST) and different stages of ocean warming simulated by climate models. We argue that the observed warming pattern is closely linked to the background circulation in the upper ocean and emerges only at the early stage of anthropogenic warming when the warming signal concentrates in the upper ocean. On centennial to millennial timescales, we expect that the warming of subpolar oceans will ultimately outpace the subtropical warming.

Results

Strong subtropical ocean warming recorded in satellite measurements. The satellite-derived SST trend (Fig. 1a) illustrates a pronounced warming over the subtropical oceans but a cooling in the eastern equatorial Pacific Ocean. This pattern closely resembles the conditions prevalent during a negative phase of the Pacific Decadal Oscillation (PDO[26]) and consequently has been widely attributed to internal climate variability[27,28]. However, strong subtropical ocean warmings are found not only in the Pacific Ocean but also across the Atlantic and Indian Oceans. These patterns persisted even during the recent positive phase of PDO (i.e., 2014–2018, Supplementary Fig. 1). This raises doubts concerning the dominance of PDO in the observed warming trend[29,30].

To illustrate this, we diminish the influence of PDO on the SST trend. The SST variability related to PDO fluctuations is identified and eliminated by a linear combination of the fingerprint and index of PDO (see "Methods"). After this approach, the amplitudes of Northern Pacific subtropical warming and eastern equatorial Pacific cooling are reduced (Fig. 2a). Nevertheless, the pattern of enhanced subtropical warming persists. Using the same approach, we can also diminish the impact of the Atlantic Multidecadal Oscillation on the SST trend. Again, the enhanced subtropical warming persists (Fig. 2b), indicating that it may be independent of internal climate variability.

The subtropical warming shows a stronger and more extensive signal in the western basins than in the eastern basins. This appears to be similar to the structure of subtropical gyres, which are illustrated by the barotropic streamfunction (Fig. 1a, contours). These subtropical gyres are characterized by the convergence of surface water and downwelling at their centers located at the western ocean basins because of the effect of 'western intensification'[31]. Previous studies[32–34] demonstrated that surface convergence is responsible for a heavy accumulation of floating marine debris over the subtropical gyres. For the same dynamical reason, under GHG-induced anomalous radiative heating, surface convergence may also contribute to fast warming over the subtropical gyres.

To verify our hypothesis, we compare the observed warming pattern with the forced warming pattern simulated by climate models. Here, we use the Coupled Model Intercomparison Project Phase 6 (CMIP6) abrupt4xCO2 experiment[35], in which the atmospheric concentration of CO_2 abruptly quadruples, and the climate thereafter adjusts to the radiative imbalance. Strong CO_2 forcing amplifies the forced response with respect to climate noises. To avoid model-dependent results, we analyze the ensemble mean results from 22 climate models (Supplementary Table 1) participating in the CMIP6.

Despite some regional discrepancies over the southern Indian Ocean and the eastern equatorial Pacific Ocean (discussed later), the abrupt4xCO2 experiment reproduces a warming pattern that resembles the observations (Fig. 1a, b). In the first year of the abrupt4xCO2 experiment, the pattern correlation is 0.53 and reaches 0.67 after a decade (Fig. 3). This is due to the development of a hemispheric asymmetry in warming with an amplified signal in the Northern Hemisphere and relatively weak warming in the Southern Hemisphere (Supplementary Fig. 2). Interestingly, this resemblance in warming patterns persists briefly over the first one to two decades of the CO_2 perturbation, but thereafter diverges from observations (Fig. 3 and Supplementary Fig. 2). Given that the abrupt4xCO2 experiment is too idealized, we also examined the other transient experiment (i.e., the 1pctCO2 experiment) with relatively mild GHG forcing. The results exhibit a similar evolution (Supplementary Fig. 3).

To further deduce whether the atmosphere or ocean dynamics are responsible for generating the enhanced subtropical warming pattern, we conducted two simulations using the Finite Element Sea Ice-Ocean Model (FESOM1.4[36]). A control simulation is performed by applying observational atmosphere forcing. A second simulation is similar to the control experiment except that the air temperature is increased uniformly by 4 K in the sea ice-free regions. We refer to this simulation as the Uniform4K experiment. As atmospheric wind, cloud, and humidity patterns may contribute to a spatially nonuniform surface heat flux to the ocean, we simplify the bulk formulation of surface heat flux[37]. In the simplified scheme, the net surface heat flux into the ocean is linearly proportional to the differences between SST and surface air temperature.

Although the uniformity in temperature anomaly applied in the Uniform4K experiment, the model simulates stronger warming in subtropical gyres where maxima align with the maxima in the streamfunction (Fig. 4). This demonstrates that the surface convergence of subtropical gyres constrains the surface warming and favors enhanced subtropical warming. It should be noted that in observations and the abrupt4xCO2 experiment, unlike in the Uniform4K experiment, the subtropical ocean warming is maximized on the polar side of the subtropical gyres (Fig. 1a, b). This discrepancy is caused by a poleward shift of the oceanic and atmospheric circulation in observations[38,39] and the abrupt4xCO2 experiment[40]. Such a shift does not appear in the Uniform4K experiment, as the wind forcing is frozen.

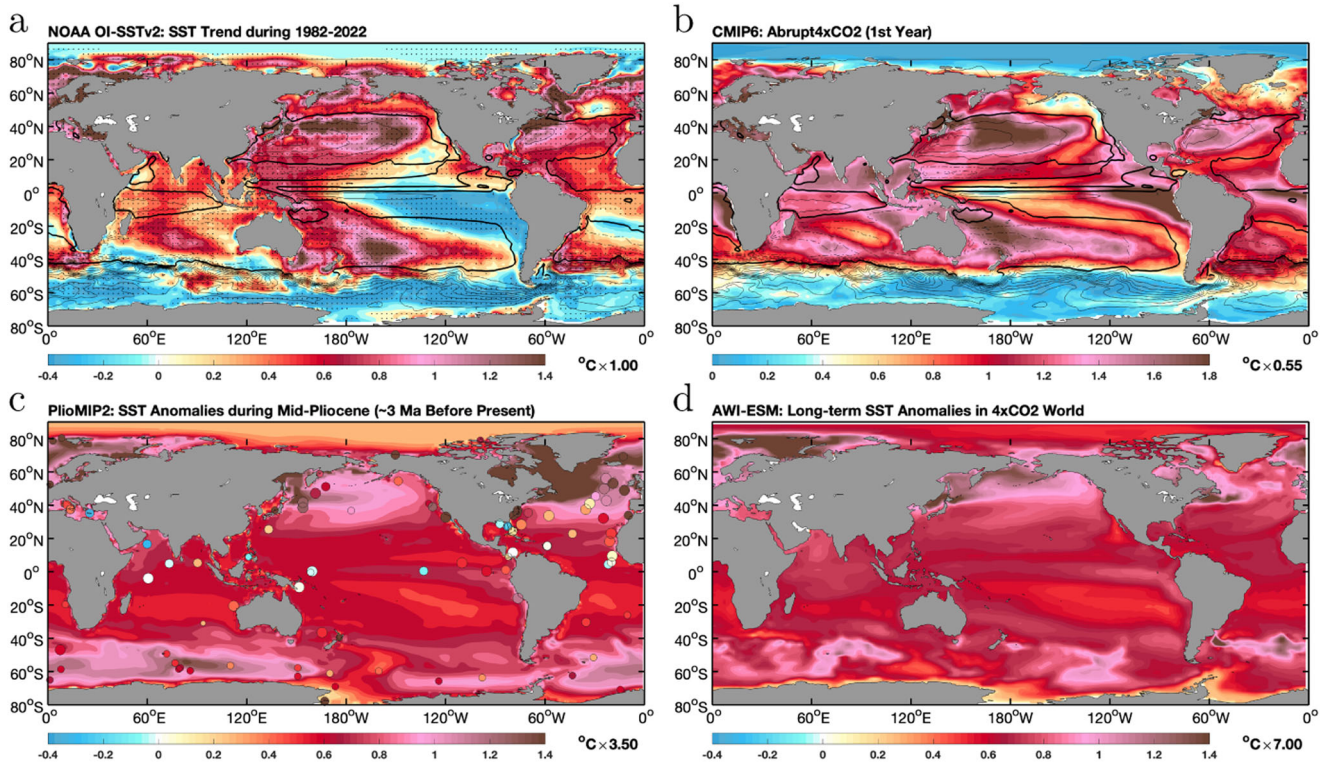

Fig. 1 Short-term and long-term ocean surface warming patterns in response to greenhouse gases (GHG) forcing. a Satellite-observed SST trend during the past 41 years (1982–2022). Stippling indicates regions where the trends pass the 95% confidence level (two-tailed Student's *t*-test). **b** Early stage of ocean surface warming in response to abruptly increased GHG. The pattern represents SST anomalies in the first year of the CMIP6 abrupt4xCO2 experiment. The position of subtropical ocean gyres is illustrated by the climatological barotropic streamfunction of the AWI-ESM pre-industrial simulation[103] (black contours). The thickened black lines mark the boundaries of ocean gyres (zeros-crossing of barotropic streamfunction). **c** Simulated SST anomalies during the mid-Pliocene. Results are based on an ensemble mean of seven models (Supplementary Table 2) that participated in the PlioMIP2[87]. Circles represent proxy-based reconstructions of SST compiled in the framework of the PRISM[78]. Circle sizes illustrate the confidence level. Small: low confidence. Medium: medium confidence. Large: High confidence. **d** Long-term ocean warming pattern under 4xCO2 forcing. Results are the last 100 years of SST anomalies from a 3000-year abrupt4xCO2 simulation conducted using AWI-ESM (see "Methods"). Note: to emphasize the spatial pattern, the color bars have been scaled. The corresponding scaling factors are given on the right side of the individual color bar.

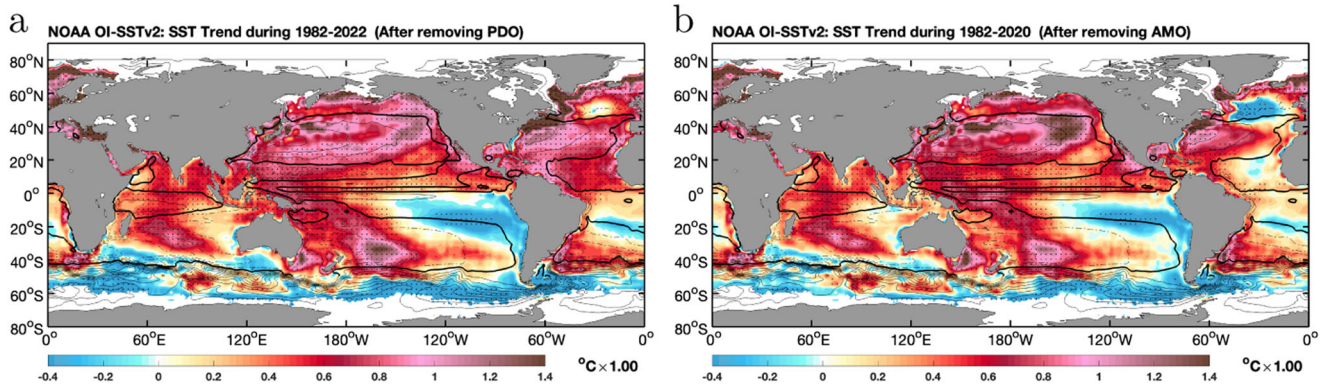

Fig. 2 Observational SST trends after removing the multidecadal climate variabilities. a SST trends after removing the PDO signal. **b** SST trends after removing the AMO signal. Stippling indicates regions where the trends pass the 95% confidence level (two-tailed Student's *t*-test). To illustrate the position of subtropical ocean gyres for comparison, we overlay the climatological barotropic streamfunction by the black contours.

To understand why ocean circulation constrains an enhanced subtropical ocean warming, we perform another coupled atmosphere-ocean simulation with an age tracer tracking the trajectory of ocean surface water. The surface water is forced to have the youngest age, i.e., 0, while the deep ocean, which has little contact with the surface, will develop the oldest age (see "Methods"). After integrating the model for 3000 years, we find that the subtropical ocean water is considerably younger (with an age of 0–5 years) than that of subpolar oceans and the eastern equatorial Pacific Ocean, where upwelling maintains older water via pumping deepwater to the surface (Fig. 5). The age pattern of the upper ocean implies that the subtropical water originates from the surface, as a result of Ekman convergence and dominant downwelling.

Constrained by upper ocean circulation, the surface radiative heating converges toward the subtropics, favoring an enhanced

subtropical ocean warming as seen in satellite measurements and the abrupt4xCO2 experiment (Fig. 1a, b).

Strongest ocean warming expected in subpolar ocean. The observed warming pattern (Fig. 1a) contradicts our understanding of how ocean temperature has changed in the geologic past. SST reconstructions covering the mid-Pliocene, the most recent time when atmospheric GHG concentrations were similar to today[41], highlight the strongest large-scale ocean warming over the subpolar oceans (Fig. 1c). Comparably, warmings in subtropical regions are less pronounced, except for the subtropical extension of western boundary currents, where a poleward shift of western boundary currents contributes to a local maximum temperature increase[8,9].

Geological reconstructions and climate simulations covering other past climate intervals, such as the Last Glacial Maximum[42,43], the Miocene[44,45], the Eocene[46], and the Cretaceous[47], also consistently suggest that subpolar ocean temperature is more sensitive to GHG forcing than subtropical ocean temperature. This robust feature is determined by several factors. First, subpolar ocean temperature is constrained by the presence of polar sea ice. Under a warming climate, sea ice loss permits the SST at high-latitude to rise more freely. Second, according to the Clausius–Clapeyron relation and the Stefan–Boltzmann law, temperature has a nonlinear relationship with evaporation and thermal radiation. It is thus more difficult to change ocean temperatures as the background temperature rises. Consequently, under anomalous radiative forcing, the subpolar ocean is expected to warm more than oceans at lower latitudes[48], whereas the warming at lower latitudes is primarily manifested by increasing humidity[49].

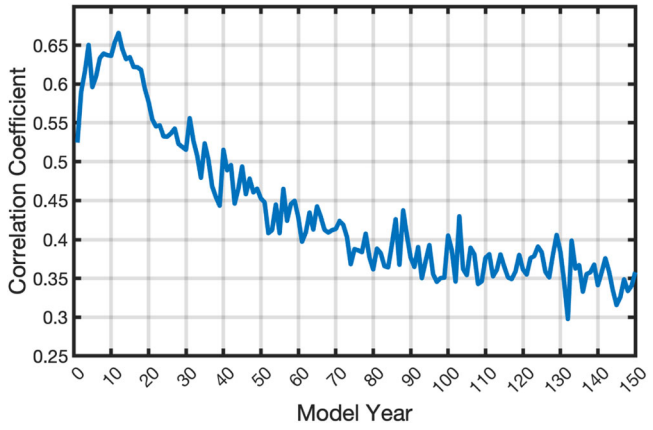

Fig. 3 Evolution of pattern correlation between observational SST trends (Fig. 1a) and simulated SST warming pattern in the CMIP6 abrupt4xCO2 experiment. The pattern correlation is calculated based on the warming pattern between 70°S and 70°N. The resemblance in the warming pattern between the observations and the model simulation is evident during the initial phase of CO_2 perturbation.

To examine how the long-term ocean warming pattern evolves in response to 4xCO2 forcing, we extend the abrupt4xCO2 experiment to 3000 years using AWI-ESM (see "Methods"). Despite extended model integration, the global mean ocean temperature continues to rise at a rate of 0.04 °C per century at the end of our simulation (Supplementary Fig. 4). This long-term ocean warming, as expected, occurs primarily in the deep ocean and at the surfaces of the subpolar ocean (Figs. 1d and 6), where surface water is connected to the deep ocean via deep convection and overturning circulation[50]. When the climate approaches a quasi-equilibrium state in response to 4xCO2 forcing, the large-scale surface warming pattern (Fig. 1d) is consistent with the mid-Pliocene warming anomaly, showing the greatest ocean warming over the subpolar regions.

According to the simulation with age tracer (Fig. 5), radiative warming can affect the subtropical upper ocean and continental shelf water quickly, i.e., within a decade. However, for the subpolar ocean, especially the Southern Ocean, the equilibrium surface warming is contingent upon the completion of deep ocean warming, a process that is projected to span multiple millennia. This distinct latitudinal difference in response time leads to enhanced subtropical warming (Figs. 1a, b, and 6a) during the initial phases of radiative forcing but amplified subpolar warming (Figs. 1c, d, and 6b) as the system approaches equilibrium.

Discussion

In this study, we evaluate the ocean warming pattern derived from four decades of satellite measurements. We find widespread strong subtropical ocean warming, concentrating mostly on the western ocean basins. In contrast to these observations, studies of paleoclimate suggest that the greatest ocean warming occurs at

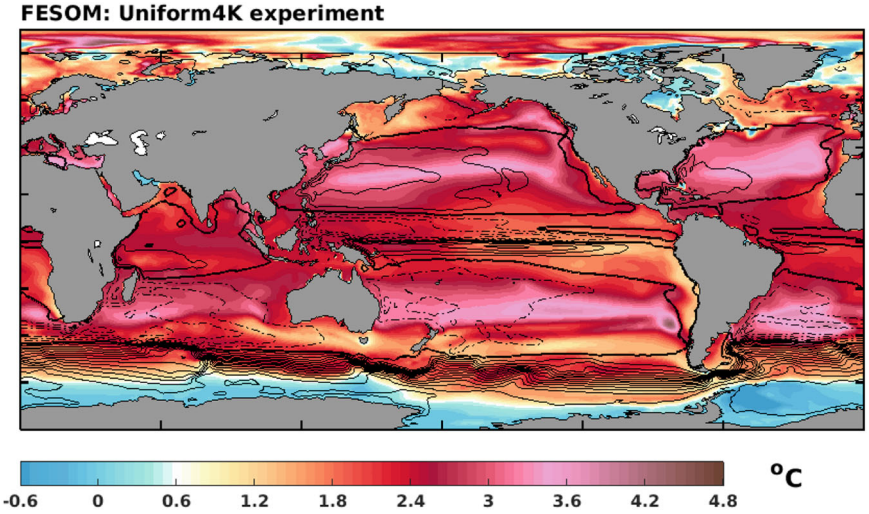

Fig. 4 SST anomalies in the Uniform4K experiment conducted by FESOM1.4. Contours illustrate the climatological barotropic streamfunction for the last 100 years of the FESOM1.4 pre-industrial control simulation. The anomalies are shown as ensemble mean of five ensemble members over their whole run time of 40 years. Despite the applied uniform warming forcing, ocean dynamics favor enhanced subtropical ocean warming.

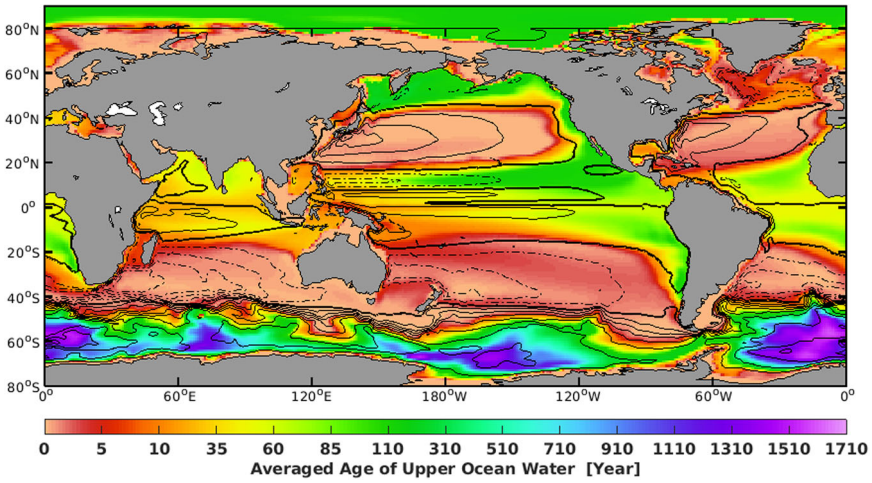

Fig. 5 Simulated averaged age of the upper 300-m ocean water column. Result based on the last 100 years of the AWI-ESM pre-industrial control simulation with ocean age tracer. The contours represent the climatological barotropic streamfunction[103], which help to illustrate the position of subtropical and subpolar gyres. The thickened black lines mark the boundaries of ocean gyres (zeros-crossing of barotropic streamfunction). The fact that the subtropical water is young implies that the water there comes from the surface of the ocean (downwelling).

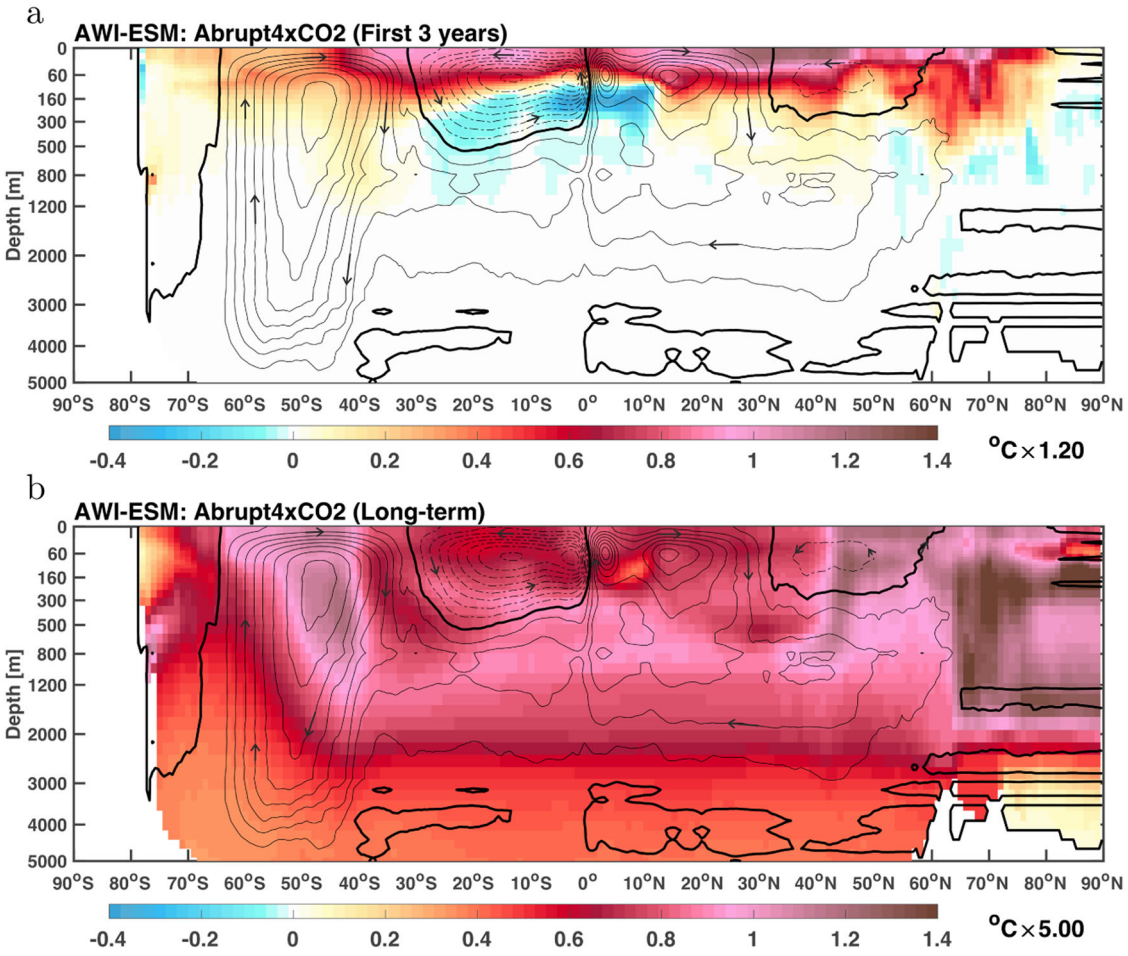

Fig. 6 The short-term and long-term ocean warming in response to abrupt4xCO2 forcing from the vertical and zonal means perspective. **a** Temperature anomalies in the very first 3 years of the AWI-ESM abrupt4xCO2 experiment with respect to the pre-industrial control experiment. **b** Temperature anomalies in the last 100 model years (2901–3000) of the AWI-ESM abrupt4xCO2 simulation with respect to the mean of the first 3 years of the same simulation. The contours illustrate the streamfunction of overturning circulation[103], solid lines represent clockwise circulation, and dashed lines stand for anti-clockwise circulation. To emphasize the spatial pattern, we show the SST anomaly using the same color bar as in Fig. 1. However, the temperature anomalies are scaled to fit the color bar range.

higher latitudes. By pairing the observed warming pattern with SST evolution in long-term climate simulations, we propose that the observed warming pattern is constrained by ocean dynamics of surface convergence (downwelling, subtropical gyres) and divergence (upwelling, subpolar gyres) rather than being dominated by internal variabilities, such as the PDO. This pattern emerges only at the early stage (a few decades) of anthropogenic warming when absorption of heat concentrates in the upper ocean. On centennial (for the Northern Pacific Ocean) to millennial (for the North Atlantic Ocean and Southern Hemisphere) timescales, when deep ocean water warms, the greatest ocean warming is expected to occur in the subpolar region, as indicated by paleo-reconstructions and the long-term and equilibrium climate simulations.

Several previous studies noticed that the mean ocean circulation affects the surface warming pattern[17,29,30]. By introducing uniform downward heat flux, Marshall et al.[17] found that the accelerating/delaying warmings in the Arctic/Antarctic are determined by the background downwelling/upwelling of Arctic/Antarctic circulation. The present study highlights that the prevailing surface convergence (downwelling) contributes to relatively fast warming over the subtropical gyres at the early stage of anthropogenic climate change. In contrast, sea ice thermodynamics and the physical law governing temperature changes prefer a subpolar amplified warming when the climate approaches an equilibrium state. The simulation with age tracer (Fig. 5) and CMIP6 simulations (Supplementary Fig. 2) suggest that the reversal of subtropical and subpolar warming patterns can be expected within a century in the North Pacific Ocean. However, the reversal of the warming pattern in the North Atlantic Ocean and Southern Hemisphere requires the warming of the deep ocean, which occurs on a millennial timescale. This is consistent with an earlier study on the equilibrium thermal response timescale of global oceans[51].

Satellite observations illustrate a reduction in SST in the southern Indian Ocean that cannot be reproduced by model simulations (Fig. 1a, b). This discrepancy may be due to the lack of iceberg activity in the CMIP6 models. Marine sediment core from the northeastern tip of the Antarctic Peninsula reveals that iceberg discharge from the Antarctic ice sheet has increased significantly in the past few millennia[52]. This contributes to regional cooling along their drift path[53]. However, CMIP6 models do not include processes of iceberg drift and melting, a circumstance that may lead to discrepancies between models and observations in the Indian Ocean.

We also note that the CMIP6 models are incapable of simulating the observed cooling in the tropical eastern Pacific Ocean (Fig. 1a, b). This discrepancy has been extensively discussed in previous literature[54–62] and is likely a consequence of a cold bias in the model's mean state of the equatorial eastern Pacific Ocean[59]. However, other factors, such as aerosol forcing[63,64], misrepresentation of the Antarctic Ozone Hole[65] or missing Antarctic meltwater impact[15,52], might also contribute to this discrepancy. Failing to capture the initial cooling signal in the tropical eastern Pacific Ocean leads to Bjerknes feedback and weaker equatorial trade winds, which can further enhance the model biases (Supplementary Fig. 2). This impact is evident in the CMIP6 historical experiment (Supplementary Fig. 5). With an improved ocean mixing scheme, part of the CMIP6 models, such as the FIO-ESM2.0[66] can simulate a cooling tropical eastern Pacific Ocean at the initial phase of GHG forcing (Supplementary Fig. 6). The abrupt CO_2 experiment performed by CESM also illustrates an initial cooling of the tropical eastern Pacific Ocean, that can be maintained only for a few decades[67]. Nevertheless, the model deficiency discussed above is unrelated to the main focus of our study, which is surface warming in the subpolar and subtropical regions.

Ocean warming pattern affects regional climate change and global climate sensitivity[29,68,69]. Recent studies[29] demonstrate that enhanced subtropical warming forces a poleward displacement of the meridional temperature gradient and, consequently, drives a poleward shift in the oceanic and atmospheric circulation[30,40]. The displacement in ocean circulation is associated with maximum warming along the oceanic subtropical fronts[39]. Thus, the observed enhanced subtropical warming is maximized toward the poleward-oriented flanks of the subtropical gyres. The PDO-like pattern drives a stronger Walker Circulation[67,70–72]. Relatively strong subtropical ocean warming sharpens mid-latitude meridional temperature gradients and intensifies westerlies and storm activity, especially in the Southern Hemisphere[50,73]. However, these changes seem to be transient. On centennial to millennial timescales, the observed strengthening of the Walker Circulation and westerlies can be reversed when ocean warming in the upwelling zones exceeds that in the downwelling zones[67,68,74,75].

Observations show that the global mean surface temperature has increased by 1.31 °C up to today[76] under the current CO_2 forcing. This estimation was for a time frame when the upwelling zones of the ocean experienced little warming or even cooling. However, this is a transient phenomenon coupled with regional ocean dynamics[10,21,50,77]. Once ocean warming reaches equilibrium, the committed warming at the current GHG level is expected to be nearly twice (2.31 °C) the recorded value (1.31 °C)[76], exceeding the Paris agreement of limiting global warming to well below 2 °C. Hence, reducing GHG levels is essential for mitigating long-term warming and keeping global warming below 2°.

Geological reconstructions and model simulations illustrate that during the mid-Pliocene when the GHG level was similar to the present, ocean temperature anomalies of about 2–5 °C occurred over the subpolar ocean[78–80]. Further back in time, during the Eocene, when the concentration of GHG was approximately 4xCO2[78], there is evidence that the ocean's deepwater was around 10 °C[81]. Given that the ocean's deepwater is formed at polar regions, this implies a high ocean temperature around both poles. Such amplified ocean warming at high latitudes has fundamental impacts on the marine-terminating ice sheets and sea level[82,83]. Subpolar ocean temperature anomalies of comparable amplitudes have neither been detected in current observations nor been projected by climate simulations at the end of this century, regardless of warming scenarios[2]. However, our work indicates that the observed ocean warming is still in its infancy. Once the high-latitude ocean warming develops, it can have irreversible consequences, such as the collapse of marine-terminating ice sheets[82], which occurred during the mid-Pliocene, along with a sea level rise of more than 10 m[84,85]. In this context, both the level and duration of elevated GHG concentrations are important in determining future climate.

Methods

We have used four kinds of data in our investigation: satellite-observed SST, multimodel simulations from the CMIP6 and PlioMIP2, mid-Pliocene SST proxies, and sensitivity simulations based on FESOM1.4 and AWI-ESM. These data and simulations are described in the following sections.

Satellite observation. The satellite-observed sea surface temperature (SST) data, i.e., NOAA OI SST V2, is used to examine the ocean warming pattern in the past four decades (1982–2022). This dataset is publicly available and provided by the NOAA/OAR/ESRL PSD, Boulder, Colorado, USA, from their website at https://www.esrl.noaa.gov/psd/.

CMIP6 data. The abrupt4xCO2 and piControl experiments from the Coupled Model Intercomparison Project (CMIP6) are used to evaluate the early stage of ocean warming response to rapidly rising greenhouse gases. In addition, the historical ssp245 and 1pctCO2 experiments are also examined in the Supplementary Information to further validate our hypothesis. Results from 47 models are included. They are listed in Supplementary Table 1. In the abrupt4xCO2 experiment, the climate simulations impose an abrupt quadrupling of the concentration of atmospheric CO_2 initialized from the piControl experiment, and that is then held fixed[35]. To calculate the CMIP6 multimodel ensemble mean, all data are interpolated onto a common $1 \times 1°$ resolution grid using bilinear interpolation.

We inspect the SST anomaly in the abrupt4xCO2 experiment with respect to the piControl experiment. The CMIP6 abrupt4xCO2 experiments are initialized at different years of the piControl simulations. In our analysis, the reference piControl climate is obtained as the three-year piControl climate around the initial condition of abrupt4xCO2 experiments. The initial condition year is identified as the year with minimum globally averaged surface salinity anomaly between the first year of abrupt4xCO2 simulations and individual year of piControl experiments.

PlioMIP2 data. The mid-Pliocene was the most recent geologic period when the GHG concentrations in the atmosphere were similar to today[41]. The mid-Pliocene SST anomaly is quantified by averaging the mid-Pliocene SST anomalies derived from 7 models that participated in the PlioMIP2. We have selected those models for which output has been freely available via the Earth System Grid Federation (https://esgf.llnl.gov/) and have also included the COSMOS as this is the PlioMIP2 ensemble member contributed by us[86]. These models are listed in Supplementary Table 2. All models provide both a Pliocene climate simulation and a corresponding pre-industrial simulation for comparison. The CO_2 level for the mid-Pliocene simulation is set to be 400 ppmv[41]. The CO_2 levels for the corresponding pre-industrial simulations are 280/284 ppmv for the non-CMIP6/CMIP6 models. Details of the modeling methodology are available from ref. [87], which describes the overall PlioMIP2 modeling strategy, and from ref. [86], which illustrates the setup of the COSMOS PlioMIP2 simulations.

Mid-Pliocene SST proxies. The Pliocene Research Interpretation and Synoptic Mapping (PRISM) database is used to evaluate the mid-Pliocene SST anomalies. This dataset includes 95 SST proxies reconstructed from three main palaeothermometers using faunal assemblages, Mg/Ca, and alkenones[78].

AWI-ESM abrupt4xCO2 simulation. The abrupt4xCO2 experiments within the CMIP6 were typically run for 150 years, which is insufficient for the climate to reach an equilibrium state. To evaluate the long-term ocean warming pattern, we conducted a 3000-year-long simulation of the abrupt4xCO2 experiment using AWI-ESM[88]. This simulation is initialized from a pre-industrial control simulation, which is also compared to the abrupt4xCO2 experiment. After 3000 years of spinup, the abrupt4xCO2 experiment reaches a quasi-equilibrium state, with radiation imbalance at the top of the atmosphere being less than 0.15 W/m^2 (Supplementary Fig. 3).

The AWI-ESM was developed by the Alfred Wegener Institute–Helmholtz-Centre for Polar and Marine Research. It consists of the atmospheric model ECHAM6[89] and the Finite volumE Sea ice-Ocean Model (FESOM), version 2[90]. The simulations performed in this study employed the AWI-ESM with an atmosphere resolution of $1.875 \times 1.875°$. The ocean model's resolution is high (approximately 25 km) near the coast, the poles, and the equator and coarse (up to 110 km) elsewhere. The atmosphere has 47 vertical levels, and the ocean has 46 vertical levels. AWI-ESM has been evaluated and widely used in the study of present and paleoclimate research[39,88,91–96].

FESOM1.4 Uniform 4 K experiment. To evaluate the ocean warming pattern under a uniform 4 K surface air temperature forcing, we conduct two simulations using the FESOM1.4[36]. The control simulation is performed based on the CORE2 climatology (1948–1999) atmospheric forcing[97]. The sensitivity experiment is exposed to an anomalous uniform 4 K surface air temperature forcing on top of the CORE2 climatology in the ice-free ocean (60°S–60°N). As atmospheric wind, cloud, and humidity patterns may contribute to a spatially nonuniform surface heat flux to the ocean, we simplify the bulk formulation of surface heat flux[37]. In our simplified heat flux scheme, the net surface heat flux into the ocean is linearly proportional to the differences between SST and surface air temperature. A similar approach has also been applied in an aqua-planet simulation[29].

The control simulation is integrated for 1000 years. The sensitivity experiment is conducted five times using different initial conditions. Each sensitivity simulation is integrated for 40 years. We evaluate the ensemble mean SST resulting from the uniform 4 K perturbation over the whole run time of the five ensemble members with respect to the last 100 years of the control simulation.

AWI-ESM simulation of ocean water age. To illustrate the circulation characteristics, a pre-industrial simulation with an age tracer is performed using the AWI-ESM. In this framework, the age tracer is set to zero in the model's ocean surface layer at each time step, and an increment equal to the model integration time is added to it below the surface[98]. Otherwise, the age tracer evolves in the ocean just like any other passive tracer, according to the same advection-diffusion equation[99]. The simulation starts with zero age everywhere in the ocean and is integrated for 3000 years. In this context, ocean water that has no contact with the surface layer has the oldest age, i.e., 3000 years, in this simulation. We examine the layer-thickness weighted average age of ocean water in the upper 300 m, which, in general, shows where the upper ocean water originates (Fig. 5).

Removal of PDO and AMO from observational SST trends. To identify and remove the PDO and AMO fluctuations from the observational records, we first identify the fingerprint of these climate modes by performing a linear regression of HadISST (1900–2021) against the PDO and AMO indices. Afterward, we reconstruct and remove the fluctuations of PDO and AMO using the following equation:

$$Y(x, y, t) = R(x, y) \cdot V(t)$$

where $Y(x, y, t)$ are the reconstructed climate variabilities related to PDO and AMO, $R(x, y)$ are the SST fingerprints of PDO and AMO, and $V(t)$ are the indices of PDO and AMO. A similar approach has also been applied by several previous studies[29,72,100]. The PDO index has been accessed from the National Centers for Environmental Information from their website at https://www.ncei.noaa.gov/access/monitoring/pdo/ (accessed on 10.02.2023). This data is based on NOAA's extended reconstruction of SSTs according to ref. [101]. The AMO Index Data is provided by the Climate Analysis Section, NCAR, Boulder, USA, in ref. [102]. (updated yearly; last accessed on 10.02.2023).

Barotropic streamfunction. The barotropic streamfunction illustrates the spatial structure of ocean gyres. It is computed by integrating the barotropic flow from north to south. Therefore, for every grid (x, y) point, the barotropic streamfunction ψ is

$$\psi(x, y) = \int_{y_0}^{y} \frac{T^x(x, y')}{\rho} dy'$$

where $T^x(x, y)$ is the depth integrated mass transport, y_0 is located at the North Pole, and ρ is the density of seawater.

Clausius–Clapeyron relations. The Clausius–Clapeyron relation describes the dependency of evaporation on temperature. It is given as:

$$lnP_{vap} = \left(\frac{-\triangle H_{vap}}{R}\right)\frac{1}{T} + C$$

where P_{vap} denotes the vapor pressure, $\triangle H_{vap}$ is the heat of vaporization, R is the gas constant, T is the temperature, and C is a constant that is specific to the liquid being examined. According to the Clausius–Clapeyron equation, the relationship between the water temperature and its vapor pressure is nonlinear. As shown by the August–Roche–Magnus equation that approximates temperature dependency of latent heat and saturation vapor pressure: for every 1 °C increase in temperature, the vapor pressure rises by around 7%. This implies that in the tropics, a specific temperature rise will cause substantially more evaporation than it does at high latitudes where temperatures are much lower.

Stefan–Boltzmann law. The Stefan–Boltzmann law describes the power radiated from a black body in terms of its temperature.

$$F = \sigma T^4$$

where F is the radiative flux, σ is the Stefan–Boltzmann constant, and T is the temperature of the black body. According to the Stefan–Boltzmann law, an increase in sea surface temperature in the warm regions (low latitudes) is much more difficult to maintain than the same temperature increase over the cold regions (high latitudes).

Data availability

The monthly sea surface temperature data (NOAA_OI_SST_V2) is provided by the NOAA/OAR/ESRL PSD, Boulder, Colorado, USA, from their website at https://www.psl.noaa.gov/data/gridded/data.noaa.oisst.v2.html. The abrupt4xCO2 and piControl experiments from the CMIP6 are publicly available for download via any one of the following portals: USA, PCMDI/LLNL (California) - https://esgf-node.llnl.gov/search/cmip6/France, IPSL - https://esgf-node.ipsl.upmc.fr/search/cmip6-ipsl/, Germany, DKRZ - https://esgf-data.dkrz.de/search/cmip6-dkrz/, UK, CEDA - https://esgf-index1.ceda.ac.uk/search/cmip6-ceda/. The mid-Pliocene model results are available from https://esgf-data.dkrz.de/search/cmip6-dkrz/. The AWI-ESM model results can be accessed at https://doi.org/10.5281/zenodo.7837865.

Code availability

The AWI-ESM code is publicly available at https://fesom.de/models/awi-cm/. The FESOM1.4 code is publicly available at https://fesom.de/models/fesom14/.

Received: 5 December 2022; Accepted: 5 May 2023;
Published online: 24 May 2023

References

1. Keeling, C. D. et al. *Exchanges of Atmospheric CO_2 and $^{13}CO_2$ with the Terrestrial Biosphere and Oceans from 1978 to 2000. I. Global Aspects* (Scripps Institution of Oceanography, 2001).
2. Masson-Delmotte, V. et al. *Climate Change 2021: The Physical Science Basis*. Contribution of Working Group I to the Sixth Assessment Report of the Intergovernmental Panel on Climate Change 2 (IPCC, 2021).
3. Fox-Kemper, B. et al. Ocean, cryosphere and sea level change in *Climate Change 2021: The Physical Science Basis*. Contribution of Working Group I to the Sixth Assessment Report of the Intergovernmental Panel on Climate Change, 1211–1362 (IPCC, 2021).
4. Woodruff, S. D. et al. ICOADS Release 2.5: extensions and enhancements to the surface marine meteorological archive. *Int. J. Climatol.* **31**, 951–967 (2011).
5. Kennedy, J. J. A review of uncertainty in in situ measurements and data sets of sea surface temperature. *Rev. Geophys.* **52**, 1–32 (2014).
6. Chan, D., Kent, E. C., Berry, D. I. & Huybers, P. Correcting datasets leads to more homogeneous early-twentieth-century sea surface warming. *Nature* **571**, 393–397 (2019).
7. Reynolds, R. W., Rayner, N. A., Smith, T. M., Stokes, D. C. & Wang, W. An improved in situ and satellite SST analysis for climate. *J. Clim.* **15**, 1609–1625 (2002).
8. Wu, L. et al. Enhanced warming over the global subtropical western boundary currents. *Nat. Clim. Change* **2**, 161–166 (2012).
9. Yang, H. et al. Intensification and poleward shift of subtropical western boundary currents in a warming climate. *J. Geophys. Res.: Oceans* **121**, 4928–4945 (2016).
10. Dima, M. & Lohmann, G. Evidence for two distinct modes of large-scale ocean circulation changes over the last century. *J. Clim.* **23**, 5–16 (2010).
11. Drijfhout, S., Van Oldenborgh, G. J. & Cimatoribus, A. Is a decline of AMOC causing the warming hole above the North Atlantic in observed and modeled warming patterns? *J. Clim.* **25**, 8373–8379 (2012).
12. Rahmstorf, S. et al. Exceptional twentieth-century slowdown in Atlantic Ocean overturning circulation. *Nat. Clim. Change* **5**, 475–480 (2015).
13. Chiang, J. C., Fang, Y. & Chang, P. Interhemispheric thermal gradient and tropical Pacific climate. *Geophys. Res. Lett.* **35**, L14704 (2008).
14. Hsiao, W.-T., Hwang, Y.-T., Chen, Y.-J. & Kang, S. M. The role of clouds in shaping tropical pacific response pattern to extratropical thermal forcing. *Geophys. Res. Lett.* **49**, e2022GL098023 (2022).
15. Kim, H., Kang, S. M., Kay, J. E. & Xie, S.-P. Subtropical clouds key to Southern Ocean teleconnections to the tropical Pacific. *Proc. Natl Acad. Sci. USA* **119**, e2200514119 (2022).
16. Hwang, Y.-T., Xie, S.-P., Deser, C. & Kang, S. M. Connecting tropical climate change with Southern Ocean heat uptake. *Geophys. Res. Lett.* **44**, 9449–9457 (2017).
17. Marshall, J. et al. The ocean's role in polar climate change: asymmetric arctic and antarctic responses to greenhouse gas and ozone forcing. *Philos. Trans. R. Soc. A: Math. Phys. Eng. Sci.* **372**, 20130040 (2014).
18. Hobbs, W. R. et al. A review of recent changes in Southern Ocean sea ice, their drivers and forcings. *Glob. Planet. Change* **143**, 228–250 (2016).
19. Meehl, G. A., Arblaster, J. M., Bitz, C. M., Chung, C. T. & Teng, H. Antarctic sea-ice expansion between 2000 and 2014 driven by tropical Pacific decadal climate variability. *Nat. Geosci.* **9**, 590–595 (2016).
20. Parkinson, C. L. A 40-y record reveals gradual Antarctic sea ice increases followed by decreases at rates far exceeding the rates seen in the Arctic. *Proc. Natl Acad. Sci. USA* **116**, 14414–14423 (2019).
21. Armour, K. C., Marshall, J., Scott, J. R., Donohoe, A. & Newsom, E. R. Southern Ocean warming delayed by circumpolar upwelling and equatorward transport. *Nat. Geosci.* **9**, 549–554 (2016).
22. Randel, W. J. & Wu, F. Cooling of the Arctic and Antarctic polar stratospheres due to ozone depletion. *J. Clim.* **12**, 1467–1479 (1999).
23. Thompson, D. W. et al. Signatures of the Antarctic ozone hole in Southern Hemisphere surface climate change. *Nat. Geosci.* **4**, 741 (2011).
24. Orr, A. et al. Strong dynamical modulation of the cooling of the polar stratosphere associated with the Antarctic ozone hole. *J. Clim.* **26**, 662–668 (2012).
25. Armour, K. C., Bitz, C. M. & Roe, G. H. Time-varying climate sensitivity from regional feedbacks. *J. Clim.* **26**, 4518–4534 (2013).
26. Mantua, N. J. & Hare, S. R. The Pacific Decadal Oscillation. *J. Oceanogr.* **58**, 35–44 (2002).
27. Allen, R. J. & Kovilakam, M. The role of natural climate variability in recent tropical expansion. *J. Clim.* **30**, 6329–6350 (2017).
28. Grise, K. M. et al. Recent tropical expansion: natural variability or forced response? *J. Clim.* **32**, 1551–1571 (2019).
29. Yang, H. et al. Tropical expansion driven by poleward advancing midlatitude meridional temperature gradients. *J. Geophys. Res.: Atmos.* **125**, e2020JD033158 (2020).
30. Yang, H., Lu, J., Wang, Q., Shi, X. & Lohmann, G. Decoding the dynamics of poleward shifting climate zones using aqua-planet model simulations. *Clim. Dyn.* **58**, 3513–3526 (2022).
31. Stommel, H. The westward intensification of wind-driven ocean currents. *Eos, Trans. Am. Geophys. Union* **29**, 202–206 (1948).
32. Law, K. L. et al. Plastic accumulation in the North Atlantic subtropical gyre. *Science* **329**, 1185–1188 (2010).
33. Eriksen, M. et al. Plastic pollution in the world's oceans: more than 5 trillion plastic pieces weighing over 250,000 tons afloat at sea. *PLoS ONE* **9**, e111913 (2014).
34. Cózar, A. et al. Plastic debris in the open ocean. *Proc. Natl Acad. Sci. USA* **111**, 10239–10244 (2014).
35. Eyring, V. et al. Overview of the Coupled Model Intercomparison Project Phase 6 (CMIP6) experimental design and organization. *Geosci. Model Dev.* **9**, 1937–1958 (2016).
36. Wang, Q. et al. The Finite Element Sea Ice-ocean Model (FESOM) v. 1.4: formulation of an ocean general circulation model. *Geosci. Model Dev.* **7**, 663–693 (2014).
37. Fairall, C. W., Bradley, E. F., Rogers, D. P., Edson, J. B. & Young, G. S. Bulk parameterization of air-sea fluxes for tropical ocean-global atmosphere coupled-ocean atmosphere response experiment. *J. Geophys. Res.: Oceans* **101**, 3747–3764 (1996).
38. Fu, Q., Johanson, C. M., Wallace, J. M. & Reichler, T. Enhanced mid-latitude tropospheric warming in satellite measurements. *Science* **312**, 1179–1179 (2006).
39. Yang, H. et al. Poleward shift of the major ocean gyres detected in a warming climate. *Geophys. Res. Lett.* **47**, e2019GL085868 (2020).
40. Yang, H., Lohmann, G., Shi, X. & Müller, J. Evaluating the mechanism of tropical expansion using idealized numerical experiments. *Ocean-Land-Atmos. Res.* **2**, 0004 (2023).
41. Badger, M. P., Schmidt, D. N., Mackensen, A. & Pancost, R. D. High-resolution alkenone palaeobarometry indicates relatively stable pCO_2 during the Pliocene (3.3–2.8 Ma). *Philos. Trans. R. Soc. A: Math. Phys. Eng. Sci.* **371**, 20130094 (2013).
42. Tierney, J. E. et al. Glacial cooling and climate sensitivity revisited. *Nature* **584**, 569–573 (2020).
43. Paul, A., Mulitza, S., Stein, R. & Werner, M. A global climatology of the ocean surface during the last glacial maximum mapped on a regular grid (GLOMAP). *Climate* **17**, 805–824 (2021).
44. Burls, N. J. et al. Simulating Miocene warmth: insights from an opportunistic multi-model ensemble (MioMIP1). *Paleoceanogr. Paleoclimatol.* **36**, e2020PA004054 (2021).
45. Frigola, A., Prange, M. & Schulz, M. Boundary conditions for the middle Miocene climate transition (MMCT v1. 0). *Geosci. Model Dev.* **11**, 1607–1626 (2018).
46. Baatsen, M. et al. The middle to late Eocene greenhouse climate modelled using the CESM 1.0.5. *Climate* **16**, 2573–2597 (2020).
47. Niezgodzki, I., Knorr, G., Lohmann, G., Tyszka, J. & Markwick, P. J. Late cretaceous climate simulations with different CO_2 levels and subarctic gateway configurations: a model-data comparison. *Paleoceanography* **32**, 980–998 (2017).
48. Pithan, F. & Mauritsen, T. Arctic amplification dominated by temperature feedbacks in contemporary climate models. *Nat. Geosci.* **7**, 181–184 (2014).
49. Song, F., Zhang, G. J., Ramanathan, V. & Leung, L. R. Trends in surface equivalent potential temperature: a more comprehensive metric for global warming and weather extremes. *Proc. Natl Acad. Sci. USA* **119**, e2117832119 (2022).
50. Yang, H., Lohmann, G., Shi, X. & Li, C. Enhanced mid-latitude meridional heat imbalance induced by the ocean. *Atmosphere* **10**, 746 (2019).
51. Yang, H. & Zhu, J. Equilibrium thermal response timescale of global oceans. *Geophys. Res. Lett.* **38**, L14711 (2011).
52. Dickens, W. et al. Enhanced glacial discharge from the eastern Antarctic peninsula since the 1700s associated with a positive southern annular mode. *Sci. Rep.* **9**, 14606 (2019).
53. England, M. R., Wagner, T. J. & Eisenman, I. Modeling the breakup of tabular icebergs. *Sci. Adv.* **6**, eabd1273 (2020).
54. Cane, M. et al. Twentieth-century sea surface temperature trends. *Science* **275**, 957–960 (1997).
55. Misra, V., Marx, L., Brunke, M. & Zeng, X. The equatorial Pacific cold tongue bias in a coupled climate model. *J. Clim.* **21**, 5852–5869 (2008).
56. Moum, J. N., Perlin, A., Nash, J. D. & McPhaden, M. J. Seasonal sea surface cooling in the equatorial Pacific cold tongue controlled by ocean mixing. *Nature* **500**, 64–67 (2013).

57. Coats, S. & Karnauskas, K. Are simulated and observed twentieth century tropical Pacific sea surface temperature trends significant relative to internal variability? *Geophys. Res. Lett.* **44**, 9928–9937 (2017).
58. Ying, J., Huang, P., Lian, T. & Tan, H. Understanding the effect of an excessive cold tongue bias on projecting the tropical Pacific SST warming pattern in CMIP5 models. *Clim. Dyn.* **52**, 1805–1818 (2019).
59. Seager, R. et al. Strengthening tropical Pacific zonal sea surface temperature gradient consistent with rising greenhouse gases. *Nat. Clim. Change* **9**, 517–522 (2019).
60. Watanabe, M., Dufresne, J.-L., Kosaka, Y., Mauritsen, T. & Tatebe, H. Enhanced warming constrained by past trends in equatorial Pacific sea surface temperature gradient. *Nat. Clim. Change* **11**, 33–37 (2021).
61. Wills, R. C., Dong, Y., Proistosecu, C., Armour, K. C. & Battisti, D. S. Systematic climate model biases in the large-scale patterns of recent sea-surface temperature and sea-level pressure change. *Geophys. Res. Lett.* **49**, e2022GL100011 (2022).
62. Park, C., Kang, S. M., Stuecker, M. F. & Jin, F.-F. Distinct surface warming response over the western and eastern equatorial Pacific to radiative forcing. *Geophys. Res. Lett.* **49**, e2021GL095829 (2022).
63. Takahashi, C. & Watanabe, M. Pacific trade winds accelerated by aerosol forcing over the past two decades. *Nat. Clim. Change* **6**, 768–772 (2016).
64. Heede, U. K. & Fedorov, A. V. Eastern equatorial Pacific warming delayed by aerosols and thermostat response to CO_2 increase. *Nat. Clim. Change* **11**, 696–703 (2021).
65. Hartmann, D. L. The Antarctic ozone hole and the pattern effect on climate sensitivity. *Proc. Natl Acad. Sci. USA* **119**, e2207889119 (2022).
66. Bao, Y., Song, Z. & Qiao, F. FIO-ESM version 2.0: model description and evaluation. *J. Geophys. Res.: Oceans* **125**, e2019JC016036 (2020).
67. Heede, U. K., Fedorov, A. V. & Burls, N. J. Time scales and mechanisms for the tropical Pacific response to global warming: a tug of war between the ocean thermostat and weaker Walker. *J. Clim.* **33**, 6101–6118 (2020).
68. Burls, N. J. & Fedorov, A. V. Wetter subtropics in a warmer world: contrasting past and future hydrological cycles. *Proc. Natl Acad. Sci. USA* **114**, 12888–12893 (2017).
69. Xie, S.-P. Ocean warming pattern effect on global and regional climate change. *AGU Adv.* **1**, e2019AV000130 (2020).
70. LHeureux, M. L., Lee, S. & Lyon, B. Recent multidecadal strengthening of the Walker circulation across the tropical Pacific. *Nat. Clim. Change* **3**, 571–576 (2013).
71. Zhao, X. & Allen, R. J. Strengthening of the Walker circulation in recent decades and the role of natural sea surface temperature variability. *Environ. Res. Commun.* **1**, 021003 (2019).
72. Heede, U. K. & Fedorov, A. V. Colder eastern equatorial Pacific and stronger Walker circulation in the early 21st century: separating the forced response to global warming from natural variability. *Geophys. Res. Lett.* **50**, e2022GL101020 (2023).
73. Chemke, R., Ming, Y. & Yuval, J. The intensification of winter mid-latitude storm tracks in the southern hemisphere. *Nat. Clim. Change* **12**, 553–557 (2022).
74. Abell, J. T., Winckler, G., Anderson, R. F. & Herbert, T. D. Poleward and weakened westerlies during Pliocene warmth. *Nature* **589**, 70–75 (2021).
75. Wu, M. et al. A very likely weakening of Pacific Walker circulation in constrained near-future projections. *Nat. Commun.* **12**, 1–8 (2021).
76. Zhou, C., Zelinka, M. D., Dessler, A. E. & Wang, M. Greater committed warming after accounting for the pattern effect. *Nat. Clim. Change* **11**, 132–136 (2021).
77. Caesar, L., Rahmstorf, S., Robinson, A., Feulner, G. & Saba, V. Observed fingerprint of a weakening Atlantic Ocean overturning circulation. *Nature* **556**, 191 (2018).
78. Dowsett, H. J. et al. Assessing confidence in Pliocene sea surface temperatures to evaluate predictive models. *Nat. Clim. Change* **2**, 365–371 (2012).
79. Foley, K. & Dowsett, H. Community sourced mid-Piacenzian sea surface temperature (SST) data. US Geological Survey data release https://doi.org/10.5066/P9YP3DTV (2019).
80. Haywood, A. M. et al. The Pliocene Model Intercomparison Project Phase 2: large-scale climate features and climate sensitivity. *Climate* **16**, 2095–2123 (2020).
81. Meckler, A. N. et al. Cenozoic evolution of deep ocean temperature from clumped isotope thermometry. *Science* **377**, 86–90 (2022).
82. Sutter, J., Gierz, P., Grosfeld, K., Thoma, M. & Lohmann, G. Ocean temperature thresholds for last interglacial West Antarctic ice sheet collapse. *Geophys. Res. Lett.* **43**, 2675–2682 (2016).
83. Miller, K. G. et al. Cenozoic sea-level and cryospheric evolution from deep-sea geochemical and continental margin records. *Sci. Adv.* **6**, eaaz1346 (2020).
84. Miller, K. G. et al. High tide of the warm Pliocene: implications of global sea level for Antarctic deglaciation. *Geology* **40**, 407–410 (2012).
85. Dumitru, O. A. et al. Constraints on global mean sea level during Pliocene warmth. *Nature* **574**, 233–236 (2019).
86. Stepanek, C., Samakinwa, E., Knorr, G. & Lohmann, G. Contribution of the coupled atmosphere–ocean–sea ice–vegetation model COSMOS to the PlioMIP2. *Climate* **16**, 2275–2323 (2020).
87. Haywood, A. M. et al. The Pliocene Model Intercomparison Project (PlioMIP) Phase 2: scientific objectives and experimental design. *Climate* **12**, 663–675 (2016).
88. Sidorenko, D. et al. Evaluation of FESOM2.0 coupled to ECHAM6.3: preindustrial and HighResMIP simulations. *J. Adv. Model. Earth Syst.* **11**, 3794–3815 (2019).
89. Stevens, B. et al. Atmospheric component of the MPI-M Earth System Model: ECHAM6. *J. Adv. Model. Earth Syst.* **5**, 146–172 (2013).
90. Danilov, S., Sidorenko, D., Wang, Q. & Jung, T. The Finite-volumE Sea ice–Ocean Model (FESOM2). *Geosci. Model Dev.* **10**, 765–789 (2017).
91. Sidorenko, D. et al. Towards multi-resolution global climate modeling with ECHAM6–FESOM. Part I: model formulation and mean climate. *Clim. Dyn.* **44**, 757–780 (2015).
92. Rackow, T. et al. Multi-resolution climate modelling with the AWI Climate Model AWI-CM-1-1. *J. Adv. Model. Earth Syst.* **12**, e2019MS002009 (2016).
93. Shi, X. & Lohmann, G. Simulated response of the mid-Holocene Atlantic meridional overturning circulation in ECHAM6-FESOM/MPIOM. *J. Geophys. Res.: Oceans* **121**, 6444–6469 (2016).
94. Shi, X., Lohmann, G., Sidorenko, D. & Yang, H. Early-Holocene simulations using different forcings and resolutions in AWI-ESM. *Holocene* **30**, 996–1015 (2020).
95. Lohmann, G., Butzin, M., Eissner, N., Shi, X. & Stepanek, C. Abrupt climate and weather changes across time scales. *Paleoceanogr. Paleoclimatology* **35**, e2019PA003782 (2020).
96. Keeble, J. et al. Evaluating stratospheric ozone and water vapour changes in CMIP6 models from 1850 to 2100. *Atmos. Chem. Phys.* **21**, 5015–5061 (2021).
97. Large, W. & Yeager, S. The global climatology of an interannually varying air–sea flux data set. *Clim. Dyn.* **33**, 341–364 (2009).
98. Thiele, G. & Sarmiento, J. Tracer dating and ocean ventilation. *J. Geophys. Res.: Oceans* **95**, 9377–9391 (1990).
99. Danabasoglu, G. et al. North Atlantic simulations in coordinated ocean-ice reference experiments phase II (CORE-II). Part I: mean states. *Ocean Model.* **73**, 76–107 (2014).
100. Ionita, M., Felis, T., Lohmann, G., Rimbu, N. & Pätzold, J. Distinct modes of East Asian Winter Monsoon documented by a southern Red Sea coral record. *J. Geophys. Res.: Oceans* **119**, 1517–1533 (2014).
101. Mantua, N. J., Hare, S. R., Zhang, Y., Wallace, J. M. & Francis, R. C. A Pacific interdecadal climate oscillation with impacts on salmon production. *Bull. Am. Meteorol. Soc.* **78**, 1069–1079 (1997).
102. Trenberth, K. E. & Shea, D. J. Atlantic hurricanes and natural variability in 2005. *Geophys. Res. Lett.* **33**, L12704 (2006).
103. Yang, H. Data for "Satellite-observed strong subtropical ocean warming as an early signature of global warming". Zenodo https://doi.org/10.5281/zenodo.7837865 (2023).

Acknowledgements

This work is supported by the AWI INSPIRES program of "Changing Earth-Sustaining our Future", PACES-II of the Helmholtz Association and Helmholtz Climate Initiative REKLIM, the Deutsche Forschungsgemeinschaft (Excellence Cluster "EXC 2077: The Ocean Floor - Earth's Uncharted Interface", project no. 390741603), and National Natural Science Foundation of China (NSFC) (grant no. 42206256, 42274094, 41941009), the Program of Marine Economy Development Special Fund under Department of Natural Resources of Guangdong Province (No. GDNRC [2022]18). We thank the climate modeling groups (listed in Supplementary Tables 1 and 2 of this paper) for producing and making available their model output.

Author contributions

H.Y. designed the study and wrote the initial draft. G.L. provided suggestions on the discussion of the manuscript. G.L., C.S., J.M., X.W., and Y.Z. assisted in the interpretation of the paleoclimate results. C.S. provided the mid-Pliocene sea surface temperature reconstructions. Q.W. helped to set up the AWI-ESM simulation with the ocean age tracer. R.H. suggested the methodology to remove the PDO signal from the original sea surface temperature data. X.S. performed the AWI-ESM pre-industrial simulation and technical support for model simulations. Y.B. provided the FIO-ESM results shown in the Supplementary Information. J.L., D.C., and Q.Y. provided discussions on the implications of the study. All authors contributed to improving the writing of the manuscript.

Funding

Open Access funding enabled and organized by Projekt DEAL.

Competing interests

The authors declare no competing interests.

Additional information

Supplementary information The online version contains supplementary material available at https://doi.org/10.1038/s43247-023-00839-w.

Correspondence and requests for materials should be addressed to Hu Yang.

Peer review information *Communications Earth & Environment* thanks Aixue Hu and the other anonymous reviewer(s) for their contribution to the peer review of this work. Primary handling editors: Regina Rodrigues, Heike Langenberg. A peer review file is available.